

# Online Generation of Collision-Free Trajectories in Dynamic Environments

Nermin Covic and Bakir Lacevic

**Abstract**—In this paper, we present an online method for converting an arbitrary geometric path represented by a sequence of states, generated by any planner (e.g., sampling-based planners like RRT or PRM, search-based planners like ARA\*, etc.), into a corresponding kinematically feasible, jerk-limited trajectory. The method generates a sequence of quintic/quartic splines that can be discretized at a user-specified control rate, and then streamed to a low-level robot controller. Our approach enables real-time adaptation to newly captured changes in the environment. It can also be re-invoked at any time instance to generate a new trajectory from the robot’s current to a desired target state or sequence of states. We can guarantee that the trajectory will remain collision-free for a certain amount of time in dynamic environments, while allowing bounded geometric deviation from the original path. The kinematic constraints are taken into account, including limited jerk. We validate the approach in a comparative simulation study against the competing method, demonstrating favorable behavior w.r.t. smoothness, computational time, and real-time performance, particularly in scenarios with frequent changes of target states (up to 1 [kHz]). Experiments on a real robot demonstrate that the proposed approach can be used in real-world scenarios including human presence.

## I. INTRODUCTION

Time-optimal path parameterization (TOPP) computes a minimum-time scaling of a collision-free path under dynamic constraints. Classical offline methods rely on *Pontryagin’s maximum principle* or *convex optimization*, including Bobrow’s algorithm [1], TOPP [2], and later TOPP-RA [3], to generate globally optimal trajectories for predefined paths. TOPP is reformulated in [4] as a convex optimal-control problem solved via second-order cone programming. Numerical-integration methods are fast but difficult to implement robustly, while convex-optimization approaches are more stable yet computationally heavier. In all cases, these techniques operate offline and assume full knowledge of the path and environment, limiting real-time adaptability.

In modern applications, however, manipulators often must replan their motions *on-the-fly* in dynamic environments (DEs) (e.g., human-robot collaboration, moving obstacles, or target changes), while guaranteeing kinematic feasibility (respecting position ( $\mathbb{P}$ ), velocity ( $\mathbb{V}$ ), acceleration ( $\mathbb{A}$ ), and jerk ( $\mathbb{J}$ ) constraints) and safety (collision avoidance, joint limits, etc.). In the sequel, *online trajectory generation* (OTG) methods for manipulators are briefly surveyed.

Many works focus on smooth, jerk-constrained trajectory generation. Quintic-polynomial-based methods produce non-oscillatory, near time-optimal motions with bounded computation by joining fifth-order polynomials between waypoints and carefully designing ramp conditions [5]. Similarly, continuous-jerk online generators based on multi-segment sine jerk profiles ensure smooth transitions under  $\mathbb{V}$  and  $\mathbb{A}$  limits [6].

Recent approaches combine piecewise sine jerk models with trapezoidal velocity transformations and smoothness coeffi-

cients to enable OTG with constant average acceleration [7]. Addressing the non-convexity introduced by third-order constraints, [8] formulates conservative inequality constraints and solves the resulting problem iteratively via an  $n$ -dimensional sequential linear programming.

Real-time and sensor-reactive OTG strategies further emphasize synchronization and computational efficiency. An S-curve-based method generates multi-DoF synchronized trajectories while minimizing either  $\mathbb{V}$  or  $\mathbb{A}$  peaks [9]. Likewise, a segment-based, dynamically adaptive look-ahead feedrate scheduler based on a *local dynamic window* and *maximum velocity curve* balances motion efficiency and stability [10]. Path-accurate trajectory generation under  $\mathbb{V}$ ,  $\mathbb{A}$ , and  $\mathbb{J}$  constraints is addressed in [11] through forward scaling and backtracking, preventing segment blending via arc-length interpolation and enabling execution at each sampling step.

Safety-aware and collision-free planning approaches extend OTG to DEs. Orthogonal collocation combined with geometric collision modeling enables smooth, time- and jerk-optimal collision-free trajectories through prescribed waypoints [12]. Autonomous reachability-based manipulator trajectory design [13] emphasizes formal safety guarantees by computing offline reachable sets and deriving provably correct online collision constraints, with fail-safe maneuvers in case of infeasibility. A two-layer architecture for human–robot collaboration adapts nominal kinodynamic trajectories to human motion while enforcing safety via velocity scaling or replanning [14].

From a computational perspective, CuRobo [15] leverages GPU acceleration to compute collision-free, minimum-jerk trajectories in tens of milliseconds through parallel inverse kinematics, collision checking, and trajectory optimization. In contrast, kinodynamic planning for multiple mobile manipulators is addressed in [16], where an offline global path is followed by an online RRT-based *receding-horizon optimizer* that jointly plans base and arm motions in DEs.

An OTG method for multi-DoF mechanical systems is presented in [17], enabling instantaneous responses to sensor events and facilitating sensor-guided motion. Building on this line of research, Ruckig [18] is introduced later as an open-source OTG library for jerk-limited, time-synchronized trajectories across multiple DoFs. Ruckig handles arbitrary initial and target states, supports asymmetric limits, and computes time-optimal trajectories in real time. Due to its computational efficiency, numerical robustness, and ease of integration, Ruckig has gained significant popularity in both academia and industry. It is widely used by over hundred research labs and open-source projects worldwide, including: MoveIt, CoppeliaSim, Frankx, etc. Thus, we adopt Ruckig as the primary benchmark in our validation study.

Tab. I summarizes the above papers. In general, online

TABLE I: Summary of key contributions of online trajectory generation and time parameterization methods.

Method	Year / Venue	Constraints	Online/ Offline	Envir. type	Safety/ Coll. aware	Optimality	Validation (Robot type)	Comput. time in [s]
Bobrow's [1]	1985 / IJRR	dynamic (torque)	offline	static	no	path-constrained, time-optimal	numerical examples (none)	n/a
TOPP [2]	1985 / T-AC	dynamic (torque)	offline	static	no	path-constrained, time-optimal	numerical examples (none)	n/a
Verschuere's [4]	2009 / T-AC	dynamic (torque)	offline	static	no	path-constrained, time-energy trade-off	simulation (6-DoF KUKA)	n/a
TOPP-RA [3]	2018 / T-RO	kin. (V, A), dyn. (torque)	offline	static	no	path-constrained, time-optimal	simulation (6-DoF arm & 50-DoF legged robot)	$\sim 10^{-2}$
ARMTD [13]	2020 / RSS	kinematic (P, V, A)	hybrid	dynamic	yes	arbitrary user-specified cost	sim. & exp. (Fetch mobile manipulator)	$\sim 10^{-1}$
Pupa's [14]	2021 / RA-L	kinematic (P, V, A)	online	dynamic	yes	max. admissible speed along the path	sim. & exp. (Pilz PRBT 6-DoF arm)	$\sim 10^{-3}$
Ruckig [18]	2021 / RSS	kinematic (P, V, A, J)	online	dynamic	no	time-optimal	sim. & exp. (Franka Panda 7-DoF arm)	$\sim 10^{-5}$
Zhao's [6]	2022 / IROS	kinematic (V, A, J)	online	dynamic	no	time-optimal within the sinusoidal-J family	sim. (UR3 arm)	n/a
CuRobo [15]	2023 / ICRA	kinematic (P, V, A, J)	online	dynamic	yes	minimum-J & minimum-A (locally)	sim. (UR5e, UR10, Kinova) & exp. (Jetson AGX)	$\sim 10^{-2}$
Patra [16]	2025 / JMR	kinodynamic (P, V, A)	hybrid	dynamic	yes	control efforts in a receding-horizon (locally)	sim. & exp. (mobile manipulator)	$\sim 10^{-1}$
<b>Splines (ours)</b>	- / -	<b>kinematic (P, V, A, J)</b>	<b>online</b>	<b>dynamic</b>	<b>yes</b>	<b>time-optimal within the parabolic-J family</b>	<b>sim. &amp; exp. (UFACTORY xArm6)</b>	$\sim 10^{-6}$

methods sacrifice global time-optimality to gain real-time reactivity and safety. Offline methods remain fastest and exact for static paths but cannot adapt to changing environments. Together, these approaches push toward the goal of real-time, guaranteed-safe trajectory generation.

This paper focuses on online time-parameterization and OTG methods that extend classical ideas to dynamic, collision-critical contexts. We highlight the following contributions:

- A new method for fast conversion of geometric paths to jerk-limited trajectories with safety guarantees in both static and dynamic environments.
- The proposed splines approach can operate with either one or more changing target waypoints.
- The method can handle arbitrary admissible initial conditions, and non-zero final velocity and acceleration values.

The next sections are organized as follows. Sec. II introduces the problem, while Sec. III briefly covers the necessary background for our approach. Then, Sec. IV describes the proposed method for local trajectory computation. Sec. V explains how geometric path can be generally converted to a corresponding trajectory. Sec. VI describes collision checking procedure for the candidate trajectory. Sec. VII deals with a comprehensive simulation study in which the proposed method is compared to a state-of-the-art algorithm. Afterward, Sec. VIII validates the novel approach on a real robot. Finally, Sec. IX brings some conclusions and future work directions.

## II. PROBLEM STATEMENT AND ASSUMPTIONS

Let  $\mathcal{C}$  denote the robot's  $n$ -dimensional configuration space. The *obstacle space*  $\mathcal{C}_{\text{obs}} \subseteq \mathcal{C}$  is the closed subset of configurations that incur collisions, either with external obstacles or by self-intersection. Its complement, the *free space*  $\mathcal{C}_{\text{free}} = \mathcal{C} \setminus \mathcal{C}_{\text{obs}}$ , is the open region of  $\mathcal{C}$  that the robot can occupy without collision. We assume that  $\mathcal{C}_{\text{obs}}$  arises from a finite collection of  $N_{\text{obs}}$  (possibly overlapping) convex *world obstacles*  $\mathcal{W}\mathcal{O}_j$ ,  $j \in \{1, \dots, N_{\text{obs}}\}$ , embedded in the robot's workspace  $\mathcal{W}$ . In situations involving non-convex obstacles, one may apply explicit decomposition methods [19]. We denote the *robot's start, current, and goal configurations* by  $\mathbf{q}_{\text{start}}$ ,  $\mathbf{q}_{\text{curr}}$ , and  $\mathbf{q}_{\text{goal}}$ , respectively.

A *motion trajectory*  $\pi(t) = \pi[\mathbf{q}_0, \mathbf{q}_f]$  is defined by a continuous mapping  $\pi : [t_0, t_f] \mapsto \mathcal{C}$  with  $\pi(t_0) = \mathbf{q}_0$  and  $\pi(t_f) = \mathbf{q}_f$ , where  $t_0$  denotes the initial time and  $t_f$  the (in general unknown) final time. Such a trajectory is deemed *valid* if  $\pi(t) \cap \mathcal{C}_{\text{obs}}(t) = \emptyset$ ,  $\forall t \in [t_0, t_f]$ , and if it can be followed by the robot under its kinematic limits and any additional constraints expressed with  $\mathcal{K}$ .

**Problem II.1.** *It is required to compute the robot's  $i$ -th joint position,  $i \in \{1, \dots, n\}$ , which can be given by an  $m$ -th order polynomial (spline) as*

$$\pi_i(t) = \xi_m^{(i)} t^m + \dots + \xi_1^{(i)} t + \xi_0^{(i)}, \quad t \in [t_0, t_{f_i}], \quad (1)$$

where  $\xi_m^{(i)}$  are (temporary) unknown coefficients, and  $t_{f_i}$  is a final time which needs to be determined. The following kinematic constraints  $\mathcal{K}$  imposed on each joint  $\mathbb{P}$ ,  $\mathbb{V}$ ,  $\mathbb{A}$ , and  $\mathbb{J}$  must be satisfied:

$$|\pi_i^{(o)}(t)| \leq q_{m_i}^{(o)}, \quad o \in \{0, 1, 2, 3\}, \quad \forall t \in [t_0, t_{f_i}], \quad (2)$$

where  $q_{m_i}^{(o)}$  represents a corresponding maximal value.

**Problem II.2.** *Let  $\mathbf{Q} = \{\mathbf{q}_1, \dots, \mathbf{q}_N\}$  be a sequence of  $N$  points/configurations from the start to the goal, where  $\mathbf{q}_1 = \mathbf{q}_{\text{start}}$  and  $\mathbf{q}_N = \mathbf{q}_{\text{goal}}$ . The aim is to time-parameterize the given path  $\mathbf{Q}$  to a corresponding collision-free trajectory  $\pi[\mathbf{q}_{\text{start}}, \mathbf{q}_{\text{goal}}]$ , which is constituted from the sequence of splines  $\mathbf{\Pi} = \{\pi[\mathbf{q}_1, \mathbf{q}_2], \dots, \pi[\mathbf{q}_{N-1}, \mathbf{q}_N]\}$ , where each spline is computed within Problem II.1, such that any constraint from  $\mathcal{K}$  must not be violated.*

**Problem II.3.** *After computing a global trajectory  $\pi[\mathbf{q}_{\text{start}}, \mathbf{q}_{\text{goal}}]$  within Problem II.2, it must be determined whether it is collision-free in the current (static) realization of the environment, or whether it will remain collision-free for a certain time in a dynamic environment.*

For the purpose of collision checking, we use bubbles of free  $\mathcal{C}$ -space that are briefly recalled in the next section. Afterward, corresponding solutions to the above-defined problems are divided into Secs. IV, V, and VI, respectively.

## III. BUBBLES OF FREE $\mathcal{C}$ -SPACE

The concept of *bubbles of free  $\mathcal{C}$ -space* was introduced in [20] as a method for defining collision-free volumes around a given configuration based on a single distance measurement from the workspace. A bubble  $\mathcal{B}(\mathbf{q}_0, d_c)$  at configuration  $\mathbf{q}_0$  is computed using the minimal distance  $d_c$  between the robot and the set of obstacles  $\mathcal{W}\mathcal{O}$  within the workspace  $\mathcal{W}$ .

**Definition III.1.** *For a robotic manipulator with  $n$  revolute joints and minimal robot-obstacle distance  $d_c$ , a bubble is formally defined as*

$$\mathcal{B}(\mathbf{q}_0, d_c) = \left\{ \mathbf{y} \mid \sum_{i=1}^n r_i |y_i - q_{0_i}| \leq d_c \right\}, \quad (3)$$

where  $r_i$  denotes the enclosing radius of a cylindrical volume aligned with the  $i$ -th joint axis, encompassing all links from joint  $i$  to the end-effector. The sum  $\sum_{i=1}^n r_i |y_i - q_{0_i}|$  is a conservative upper bound on the displacement of any point on the manipulator when the configuration changes from  $\mathbf{q}_0 = [q_1, \dots, q_n]$  to  $\mathbf{y} = [y_1, \dots, y_n]$ . During the transition from  $\mathbf{q}_0$  to any  $\mathbf{y} \in \mathcal{B}(\mathbf{q}_0, d_c)$ , no point on the kinematic chain will experience a displacement greater than  $d_c$ , ensuring that

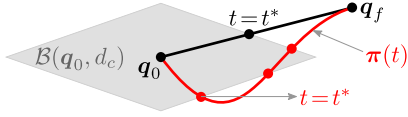


Fig. 1: Bubble  $\mathcal{B}(q_0, d_c)$  at the configuration  $q_0$  with the spine  $\overline{q_0 q_f}$  and the local trajectory  $\pi(t)$ .

*no collision occurs. From (3), it follows that bubbles have a diamond-like shape in  $\mathcal{C}$ -space.*

Clearly, we want to move from  $q_0$  towards  $q_f$  as far as possible in terms of both time and safety (i.e., retaining collision-free motion). For instance, if we set  $y(t) = q_0 + t(q_f - q_0)$  (a straight-line segment  $\overline{q_0 q_f}$ ), where  $q_f$  is a final/remote/distant configuration (e.g., Fig. 1), it yields the maximal value for the parameter  $t$  as  $t^* = \frac{d_c}{\sum_{i=1}^n r_i |q_{f_i} - q_{0_i}|}$ . Thus, the straight-line segment  $\overline{q_0 y(t^*)}$  is called *spine*.

On the other hand, if we choose a nonlinear function as  $y = \pi(t)$  (e.g., polynomial in Fig. 1), where  $\pi(t) = \pi[q_0, q_f]$ , computing  $t^*$  becomes more difficult. More precisely, computing the intersection of  $\pi(t)$  with the border of  $\mathcal{B}(q_0, d_c)$  is obtained by solving the system of equations  $\sum_{i=1}^n r_i |\pi_i(t) - q_{0_i}| = d_c$ . Multiple solutions may exist due to the nonlinear nature of  $\pi(t)$  (e.g., three red points in Fig. 1). Clearly, the smallest positive  $t$  is relevant. Since computing  $t^*$  exactly can be expensive, we present a computationally convenient workaround in Sec. VI.

#### IV. METHOD FOR SPLINE COMPUTATION

This section describes the proposed method simply referred to as CFS45 (Collision-Free 4<sup>th</sup>/5<sup>th</sup> order Splines). It computes a  $k$ -th spline  $\pi(t) = \pi[q_k, q_{k+1}]$ ,  $k \in \{1, \dots, N-1\}$ , from the sequence  $\Pi$  as described within Problem II.1.

##### A. Description of the Proposed Approach

In order to satisfy (2), it is sufficient to choose  $m = 5$  within (1) to obtain quintic spline for the robot's  $i$ -th joint as

$$\pi_i(t) = a_i t^5 + b_i t^4 + c_i t^3 + d_i t^2 + e_i t + f_i, \quad t \in [t_0, t_{f_i}], \quad (4)$$

where  $a_i = \xi_5^{(i)}$ ,  $b_i = \xi_4^{(i)}$ ,  $c_i = \xi_3^{(i)}$ ,  $d_i = \xi_2^{(i)}$ ,  $e_i = \xi_1^{(i)}$ , and  $f_i = \xi_0^{(i)}$ . Initial boundary conditions at  $t_0 = 0$  are:

$$\pi_i(0) = f_i, \quad \dot{\pi}_i(0) = e_i, \quad \ddot{\pi}_i(0) = 2d_i, \quad (5)$$

which are known from  $(k-1)$ -st spline, thus they immediately yield coefficients  $d_i$ ,  $e_i$ , and  $f_i$ . Combining final boundary conditions at  $t = t_{f_i}$ :

$$\pi_i(t_{f_i}) = \pi_{f_i} = a_i t_{f_i}^5 + b_i t_{f_i}^4 + c_i t_{f_i}^3 + d_i t_{f_i}^2 + e_i t_{f_i} + f_i, \quad (6)$$

$$\dot{\pi}_i(t_{f_i}) = \dot{\pi}_{f_i} = 5a_i t_{f_i}^4 + 4b_i t_{f_i}^3 + 3c_i t_{f_i}^2 + 2d_i t_{f_i} + e_i, \quad (7)$$

$$\ddot{\pi}_i(t_{f_i}) = \ddot{\pi}_{f_i} = 20a_i t_{f_i}^3 + 12b_i t_{f_i}^2 + 6c_i t_{f_i} + 2d_i, \quad (8)$$

the following relations can be obtained:

$$c_i t_{f_i}^3 + \left(3d_i - \frac{\ddot{\pi}_{f_i}}{2}\right) t_{f_i}^2 + (6e_i + 4\dot{\pi}_{f_i}) t_{f_i} + 10(f_i - \pi_{f_i}) = 0, \quad (9)$$

$$b_i = \frac{1}{t_{f_i}^3} \left[ -\frac{3}{2} c_i t_{f_i}^2 + \left( -\frac{3}{2} d_i - \frac{\ddot{\pi}_{f_i}}{4} \right) t_{f_i} - e_i + \dot{\pi}_{f_i} \right], \quad (10)$$

$$a_i = \frac{1}{20t_{f_i}^3} \left[ -12b_i t_{f_i}^2 - 6c_i t_{f_i} - 2d_i + \ddot{\pi}_{f_i} \right]. \quad (11)$$

The jerk function for  $i$ -th robot's joint is given as

$$\dddot{\pi}_i(t) = 60a_i t^2 + 24b_i t + 6c_i. \quad (12)$$

Since the following holds (see (2)):

$$|\ddot{\pi}_i(0)| = |6c_i| \leq \ddot{q}_{m_i} \implies c_i \in \left[ -\frac{\ddot{q}_{m_i}}{6}, \frac{\ddot{q}_{m_i}}{6} \right], \quad (13)$$

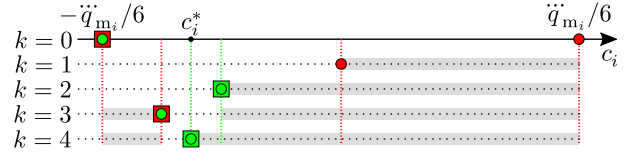


Fig. 2: Proof of concept for obtaining an optimal value for  $c_i^*$  through five iterations. Legend:  $\bullet / \bullet$  – feasible candidate of  $t_{f_i}$  exists / does not exist;  $\blacksquare / \blacksquare$  – constraints  $\mathcal{K}$  are satisfied / not satisfied.

#### Algorithm 1: Jerk Selection via Bisection Method

---

**Input:**  $c_{i,\text{left}}^{(0)} = -\frac{\ddot{q}_{m_i}}{6}$ ,  $c_{i,\text{right}}^{(0)} = \frac{\ddot{q}_{m_i}}{6}$ ,  $\Delta c_i$   
**Output:**  $c_i^*$ ,  $t^*$

- 1  $c_i^* \leftarrow \emptyset$ ,  $t^* \leftarrow \emptyset$ ,  $k \leftarrow 1$
- 2  $t_{f_i} \leftarrow \text{computeRealCandidates}(c_{i,\text{left}}^{(0)}, c_{i,\text{right}}^{(0)})$
- 3 **if** exists feasible  $t_{f_i}$  **then**
- 4     **if** satisfies  $\mathcal{K}$  for  $c_{i,\text{left}}^{(0)}$  or  $c_{i,\text{right}}^{(0)}$  **then**
- 5          $t^*$ ,  $c_i^* \leftarrow \text{getMinimalFeasible}(t_{f_i}, c_i)$
- 6         **return**  $c_i^*$ ,  $t^*$
- 7     **else**
- 8         **return** No solution can be found!
- 9     **if not** satisfy  $\mathcal{K}$  for  $c_{i,\text{right}}^{(0)}$  **then**
- 10         left, right  $\leftarrow$  right, left // switch sides
- 11 **else**
- 12     **return** No solution can be found!
- 13 **while**  $c_{i,\text{right}}^{(k-1)} - c_{i,\text{left}}^{(k-1)} > \Delta c_i$  **do**
- 14      $c_i^{(k)} \leftarrow (c_{i,\text{left}}^{(k-1)} + c_{i,\text{right}}^{(k-1)}) / 2$
- 15      $c_{i,\text{left}}^{(k)} \leftarrow c_{i,\text{left}}^{(k-1)}$ ,  $c_{i,\text{right}}^{(k)} \leftarrow c_i^{(k)}$
- 16      $t_{f_i} \leftarrow \text{computeRealCandidates}(c_i^{(k)})$
- 17     **if** exists feasible  $t_{f_i}$  **then**
- 18         **if** satisfies  $\mathcal{K}$  **then**
- 19              $t^*$ ,  $c_i^* \leftarrow \text{getMinimalFeasible}(t_{f_i}, c_i^{(k)})$
- 20         **else**
- 21              $c_{i,\text{left}}^{(k)} \leftarrow c_i^{(k)}$ ,  $c_{i,\text{right}}^{(k)} \leftarrow c_{i,\text{right}}^{(k-1)}$
- 22      $k \leftarrow k + 1$
- 23 **return**  $c_i^*$ ,  $t^*$

---

we can pick  $c_i$  from such range and then compute  $t_{f_i}$  from (9) by solving the cubic equation (either numerically or exactly using Cardano's formula). Then, for each positive real solution  $t_{f_i}$ , (10) provides  $b_i$ , and finally (11) yields  $a_i$ .

After computing coefficients  $a_i, b_i, c_i, d_i, e_i, f_i$  and final time  $t_{f_i}$ , we must verify kinematic constraints by (2). According to (5)–(8), all boundary conditions for  $t = 0$  and  $t = t_{f_i}$  are satisfied for  $\mathbb{P}$ ,  $\mathbb{V}$ , and  $\mathbb{A}$ . However, jerk values  $\ddot{\pi}_i(0)$  and  $\ddot{\pi}_i(t_{f_i})$  need to be verified. Instead of checking (2)  $\forall t \in (0, t_{f_i})$ , it suffices to verify at candidate extremal times, i.e., to solve  $\dot{\pi}_i(t) = 0$ ,  $\ddot{\pi}_i(t) = 0$ ,  $\ddot{\pi}_i(t) = 0$ , and  $q_i^{(4)}(t) = 0$  to obtain time instances  $t_{m,\text{pos}}$ ,  $t_{m,\text{vel}}$ ,  $t_{m,\text{acc}}$  and  $t_{m,\text{jerk}}$  of maximal  $\mathbb{P}$ ,  $\mathbb{V}$ ,  $\mathbb{A}$ , and  $\mathbb{J}$ , respectively, and evaluate constraints there. If any constraint is violated, the guess for  $c_i$  must be changed (as it will be described in Subsec. IV-B), after which  $t_{f_i}$ ,  $b_i$ , and  $a_i$  must be computed again until (2) holds. In case the synchronization of all joints is desired, the final time is chosen as  $t_f = \max\{t_{f_1}, \dots, t_{f_n}\}$ , upon which all coefficients  $a_i, b_i$ , and  $c_i$  are recomputed and all  $\mathcal{K}$  verified.

Finally, it is worth stressing that the same logic is utilized to compute quartic splines (for  $m = 4$  within (1)), which are

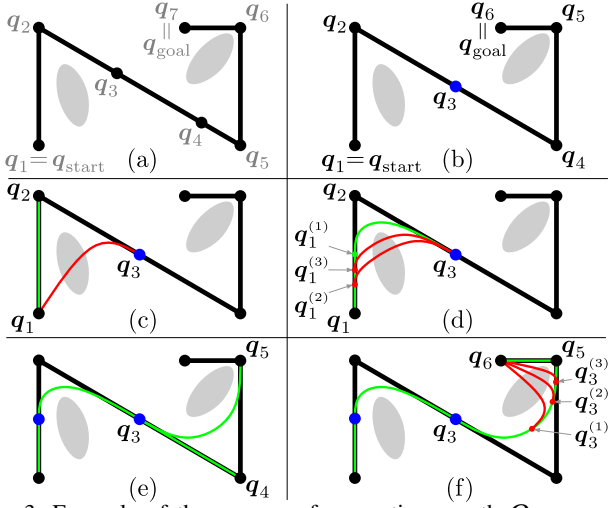


Fig. 3: Example of the process of converting a path  $Q : q_{\text{start}} \rightarrow q_{\text{goal}}$  (black) to a corresponding trajectory (green).

used for the robot's emergency stopping when computing safe trajectories (see Sec. VI). The only difference is that the final position (within (6)) is free and is computed as a consequence.

### B. Jerk Selection via Bisection Method

Alg. 1 describes the procedure for obtaining an optimal value for  $c_i^*$ , while Fig. 2 demonstrates the proof of concept in the worst-case scenario. Initially, line 2 checks boundary points in the iteration  $k = 0$ , i.e., for  $c_{i,\text{left}}^{(0)} = -\ddot{q}_{m_i}/6$  and  $c_{i,\text{right}}^{(0)} = \ddot{q}_{m_i}/6$ . In case real solutions for  $t_{f_i}$  exist for both or one of  $c_i^{(0)}$ , and  $\mathcal{K}$  are satisfied at the same time, we choose the solution with minimal  $t_{f_i}$  by line 5. For instance, Fig. 2 depicts the situation (in case  $k = 0$ ) for  $c_{i,\text{right}}^{(0)}$  when neither of real solutions for  $t_{f_i}$  exist. Conversely, the real solutions for  $c_{i,\text{left}}^{(0)}$  exist, but  $\mathcal{K}$  are not satisfied for any of them.

Therefore, in the subsequent iterations (i.e.,  $k \geq 1$  by lines 13–22), we use bisection method to find a new value for  $c_i^{(k)}$ ,  $k \geq 1$ , by line 14. Clearly, due to the symmetric jerk limits,  $c_i^{(1)} = 0$  holds. Without the loss of generality, let us assume that real solution for  $t_{f_i}$  does not exist (as indicated by Fig. 2), thus the range  $[0, c_{i,\text{right}}^{(0)}]$  will not yield solution and it is eliminated (e.g., marked gray in Fig. 2). Therefore, we set  $c_{i,\text{left}}^{(1)} = c_{i,\text{left}}^{(0)}$ ,  $c_{i,\text{right}}^{(1)} = c_i^{(1)}$  and then check for  $c_i^{(2)}$ . Fig. 2 reveals that the real  $t_{f_i}$  exists with  $\mathcal{K}$  not being violated, thus  $c_{i,\text{left}}^{(2)} = c_{i,\text{left}}^{(1)}$  and  $c_{i,\text{right}}^{(2)} = c_i^{(2)}$ . However, we seek for other solutions from the range  $[c_{i,\text{left}}^{(2)}, c_{i,\text{right}}^{(2)}]$  since they can provide smaller values for  $t_{f_i}$ . After obtaining  $c_i^{(3)}$ , Fig. 2 shows that  $\mathcal{K}$  are violated, thus  $c_{i,\text{left}}^{(3)} = c_i^{(3)}$  and  $c_{i,\text{right}}^{(3)} = c_{i,\text{right}}^{(2)}$ . Finally,  $c_i^{(4)}$  provides real  $t_{f_i}$  and satisfies  $\mathcal{K}$ . The procedure can continue until the remaining range width of  $c_{i,\text{right}}^{(k)} - c_{i,\text{left}}^{(k)}$  drops below a given threshold (*jerk precision*  $\Delta c_i$  in line 13).

## V. PATH-TO-TRAJECTORY CONVERSION

This section is concerned with converting an arbitrary, collision-free, geometric path  $q_{\text{start}} \rightarrow q_{\text{goal}}$  to a corresponding trajectory, i.e., to a sequence of splines  $\Pi$ , as described within Problem II.2. To facilitate the understanding of this process, we will refer to Alg. 2 and Fig. 3 in the sequel. The

### Algorithm 2: Path-to-Trajectory Conversion

---

**Input:** Geometric path  $Q = \{q_1, \dots, q_N\}$ ,  $D_{\text{max}}$   
**Output:** Spline sequence  $\Pi$

- 1  $Q \leftarrow \text{simplify\&Densify}(Q) // \text{ s.t. } \|q_{k+1} - q_k\| \leq D_{\text{max}}$
- 2  $\Pi \leftarrow \emptyset$ ,  $k \leftarrow 1$
- 3 **while**  $k < \text{size}(Q) - 1$  **do**
- 4      $\pi_{k,k+2} \leftarrow \text{computeSpline}(q_k, q_{k+2}, \dot{q}_{k+2})$
- 5     **if**  $\pi_{k,k+2}$  is collision-free **then**
- 6          $\Pi \leftarrow \Pi \cup \pi_{k,k+2}$ ,  $k \leftarrow k + 2$
- 7     **else**
- 8          $\pi_{k,k+1} \leftarrow \text{computeSpline}(q_k, q_{k+1}, \dot{q}_{k+1})$
- 9          $\pi_{k,k+2} \leftarrow \text{bisection}(\pi_{k,k+1}, q_{k+2})$
- 10         **if**  $\pi_{k,k+2}$  is found **then**
- 11              $\Pi \leftarrow \Pi \cup \pi_{k,k+2}$ ,  $k \leftarrow k + 2$
- 12         **else**
- 13              $\Pi \leftarrow \Pi \cup \pi_{k,k+1}$ ,  $k \leftarrow k + 1$
- 14 **if**  $k = \text{size}(Q) - 1$  **then**
- 15      $\pi_{k,k+1} \leftarrow \text{computeSpline}(q_k, q_{k+1}, \dot{q}_{k+1} = 0)$
- 16      $\Pi \leftarrow \Pi \cup \pi_{k,k+1}$
- 17 **return**  $\Pi$

---

geometric path  $Q : q_{\text{start}} \rightarrow q_{\text{goal}}$  can be computed by any planner (e.g., RRT-Connect [21]).

First, the procedure begins with line 1 by reallocating nodes on the path such that the Euclidean-base distance between two consecutive nodes does not exceed  $D_{\text{max}}$ , which represents a user-defined parameter. The goal is to minimize the number of path nodes without changing its geometrical shape (e.g., intermediate nodes  $q_3$  and  $q_4$  from a straight-line segment are replaced with a new  $q_3$ , as depicted in blue by Fig. 3 (a)). Particularly, when the proposed approach is applied to a real-time algorithm (e.g., RRT<sup>X</sup> [22], MARS [23], or DRGBT [24]),  $D_{\text{max}}$  can be computed as  $\|\dot{q}_{\text{max}}\| \cdot T$ , where  $T$  represents the *planner's iteration time*.

Afterward, the sequence of splines  $\Pi$  is being computed within lines 3–16. At each iteration, we attempt to compute a spline from  $q_k$  toward  $q_{k+2}$ ,  $k \in \{1, \dots, N - 2\}$ , as an attempt to interpolate the path (if possible) around the *corner point*  $q_{k+1}$ . It is worth indicating that  $\nabla$  and  $\mathbb{A}$  at the black points in Fig. 3 are always zero, while  $\nabla$  at the blue points can be generally non-zero since they lie on a straight-line segment. The  $\nabla$  at the blue point  $q_k$  is estimated as  $\dot{q}_k = (q_{k+1} - q_k)/t$ , where  $t$  is picked from the range  $(0, T]$  in order to keep  $q_k$  feasible (e.g., used within lines 4 and 8).

First, line 4 computes the spline  $\pi_{k,k+2} = \pi[q_k, q_{k+2}]$  (e.g., the red line in Fig. 3 (c) for  $k = 1$ ) and checks it for collision by line 5. If it is collision-free, it will be stored in  $\Pi$ , and line 4 will compute the next spline (e.g.,  $\pi_{3,5}$  in Fig. 3 (e)). Otherwise, line 8 computes the spline  $\pi_{k,k+1} = \pi[q_k, q_{k+1}]$  (e.g.,  $\pi_{1,2}$  in Fig. 3 (c)), which is always feasible since boundary  $\nabla$  and  $\mathbb{A}$  are satisfied, i.e., zero.

Let us assume that  $\pi_{k,k+2}$  is in collision (as depicted for  $\pi_{1,3}$  by Fig. 3 (c)). Then, line 9 searches for the collision-free spline  $\pi[q_k, q_{k+2}]$ , so-called *interpolating spline*, that lies between  $\pi_{k,k+1}$  and  $\pi_{k,k+2}$ , which is as close as possible to  $\pi_{k,k+2}$ . We utilize the bisection method as follows. The first *intermediate node* is selected as  $q_k^{(1)} = \pi_{k,k+1}(t_k^{(1)})$ , where  $t_k^{(1)} = \frac{t_k + t_{k+1}}{2}$ ,  $q_k = \pi_{k,k+1}(t_k)$ , and  $q_{k+1} = \pi_{k,k+1}(t_{k+1})$ .

---

**Algorithm 3:** Bur – computeBur

---

**Input:**  $\pi_{\text{reg}}(t) = \pi[\mathbf{q}_0, \mathbf{q}_f]$ ,  $\Delta t$ ,  $\mathbf{d}(t_0)$   
**Output:**  $Bur$

- 1  $Q, Bur \leftarrow \emptyset$ ,  $k \leftarrow 0$
- 2 **while**  $k\Delta t < \text{getTime}(\mathbf{q}_f)$  **do**
- 3      $Q \leftarrow [Q, \pi_{\text{reg}}(k\Delta t)]$
- 4      $k \leftarrow k + 1$
- 5  $Q \leftarrow [Q, \mathbf{q}_f]$
- 6  $\mathcal{B}_0 \leftarrow \mathcal{B}(\mathbf{q}_0, \mathbf{d}(t_0))$
- 7 **for**  $k = 1 : \text{size}(Q)$  **do**
- 8     **if**  $\mathbf{q}_k \in \mathcal{B}_0$  **then**
- 9          $Bur \leftarrow [Bur, \overline{\mathbf{q}_0\mathbf{q}_k}]$
- 10     **else**
- 11         **return**  $Bur$

---

Then, the spline  $\pi[\mathbf{q}_k^{(1)}, \mathbf{q}_{k+2}]$  is checked for collision (as shown by Fig. 3 (d) for  $\pi[\mathbf{q}_{1,1}, \mathbf{q}_3]$ ). If it is collision-free, we seek for the second intermediate node  $\mathbf{q}_k^{(2)} = \pi_{1,2}(t_k^{(2)})$ , where  $t_k^{(2)} = \frac{t_k + t_k^{(1)}}{2}$ . Otherwise,  $t_k^{(2)} = \frac{t_k^{(1)} + t_{k+1}}{2}$ . Hence, the procedure is repeated until the change of  $t_k^{(\cdot)}$  (e.g.,  $|t_k^{(2)} - t_k^{(1)}|$ ) becomes less than a specified threshold.

Fig. 3 (e) shows the computed splines  $\pi[\mathbf{q}_3, \mathbf{q}_4]$  and  $\pi[\mathbf{q}_3, \mathbf{q}_5]$ . They are both feasible, thus the second one is chosen. Since  $\mathbf{q}_5$  is the corner point, we seek for an interpolating spline toward  $\mathbf{q}_6$  using the bisection method, as depicted by Fig. 3 (f). It can occur that such spline cannot be found, thus the robot will move to  $\mathbf{q}_5$ , stop in  $\mathbf{q}_5$ , and then change direction to follow the spline  $\pi[\mathbf{q}_5, \mathbf{q}_6]$  (computed by line 15 since  $\mathbf{q}_6 = \mathbf{q}_{\text{goal}}$  in Fig. 3 (f)). Therefore, the solution always exist and the robot can successfully reach the goal. In the worst-case scenario (i.e., when the interpolation is not possible), the obtained trajectory (shown in green) will geometrically correspond to the initial path (depicted in black).

The procedure in Alg. 2 represents a general framework suitable for static environments. It can also be applied in DEs if the used dynamic planner is able to timely supply a sequence of targets (waypoints). However, in dynamic settings, it is often computationally inefficient to track multiple future targets because they generally move in time according to changes in the environment. For the sake of meeting real-time constraints, it is sometimes necessary to account only for a single target  $\mathbf{q}_{\text{target}}$  (the immediate next one) even in case when a fully predefined path to the goal is available.

For instance, to enable smooth trajectory interpolation, DRGBT [24] does not wait for the robot to exactly reach  $\mathbf{q}_{\text{target}}$ . Instead, once the robot approaches this configuration within an Euclidean distance defined by  $n \cdot R \cdot \|\dot{\mathbf{q}}_{\text{curr}}\| / \|\dot{\mathbf{q}}_{\text{m}}\|$ , where  $R$  is a user-defined parameter, the target is considered reached, thus DRGBT is allowed to request a new target. Generally, the target may be updated at each iteration if a dynamic planner decides that such change is necessary.

## VI. TRAJECTORY COLLISION CHECKING

This section addresses Problem II.3, i.e., it describes how a single spline from the sequence  $\mathbf{\Pi}$  can be checked for collision. Suppose that such spline is given as  $\pi_{\text{reg}}(t) = \pi[\mathbf{q}_0, \mathbf{q}_f]$  for  $t \in [t_0, t_f]$ , and is called a *local regular trajectory* (e.g., the blue spline in Fig. 4 (a)).

---

**Algorithm 4:** Generalized bur – computeGBur

---

**Input:**  $\pi_{\text{reg}}(t) = \pi[\mathbf{q}_0, \mathbf{q}_f]$ ,  $\Delta t$ ,  $\mathbf{d}(t_0)$   
**Output:**  $GBur$

- 1  $GBur \leftarrow \emptyset$ ,  $k \leftarrow 0$
- 2 **while**  $\mathbf{q}_k \neq \mathbf{q}_f$  **do**
- 3      $Bur_k \leftarrow \text{computeBur}(\pi[\mathbf{q}_k, \mathbf{q}_f], \Delta t, \mathbf{d}(t_k))$
- 4     **if**  $Bur_k \neq \emptyset$  **then**
- 5          $\overline{\mathbf{q}_k\mathbf{q}_m} \leftarrow Bur_k(\text{end})$
- 6          $t_m \leftarrow \text{getTime}(\mathbf{q}_m)$
- 7          $\mathbf{d}(t_m) \leftarrow \text{getDistancesToPlanes}(\mathbf{q}_m, \mathcal{P}(t_m))$
- 8          $GBur \leftarrow [GBur, Bur_k]$
- 9          $k \leftarrow m$
- 10     **else**
- 11         **return**  $GBur$

---

The proposed procedure given in Alg. 3 involves the following steps:

**Step 1** (lines 1–5): Discretize the spline  $\pi_{\text{reg}}(t)$  with a step  $\Delta t$  to obtain *intermediate configurations*  $\mathbf{q}_k = \pi_{\text{reg}}(k\Delta t)$ ,  $k = \{1, \dots, N\}$  (e.g., nodes  $\mathbf{q}_1, \dots, \mathbf{q}_{10}$  in Fig. 4 (a)).

**Step 2** (line 6): Compute the bubble  $\mathcal{B}(\mathbf{q}_0, \mathbf{d}(t_0)) \equiv \mathcal{B}_0$  at the root  $\mathbf{q}_0$  using the vector of minimal distances  $\mathbf{d} = \mathbf{d}(t_0) = [d_1, \dots, d_n]^T$  for each robot’s link as proposed in [25].

**Step 3** (lines 7–11): Simply check which intermediate nodes lie within  $\mathcal{B}_0$ . If (3) is satisfied, the spine  $\overline{\mathbf{q}_0\mathbf{q}_k}$  is collision-free for  $t \in [t_0, t_f]$ , i.e.,  $\overline{\mathbf{q}_0\mathbf{q}_k} \in \mathcal{B}_0$ , (e.g., spines  $\overline{\mathbf{q}_0\mathbf{q}_1}, \dots, \overline{\mathbf{q}_0\mathbf{q}_3}$  from Fig. 4 (a)). Otherwise, it implies that all nodes  $\mathbf{q}_p \notin \mathcal{B}_0$ ,  $\forall p \in \{k, \dots, N\}$ , (e.g., nodes  $\mathbf{q}_4, \dots, \mathbf{q}_{10}$  in Fig. 4 (a)). The collection of spines  $\overline{\mathbf{q}_0\mathbf{q}_k} \in \mathcal{B}_0$  is an instance of the structure called *bur of free C-space (Bur)* [26].

The described procedure yields an approximate  $t^* \approx t_{k-1}$  (see Fig. 1) (e.g.,  $t^* \approx t_3$  in Fig. 4 (a)).

### A. Further Exploration of C-space

After reaching the border of the bubble  $\mathcal{B}_0$  (e.g.,  $\mathbf{q}_3$  in Fig. 4 (a)), spines  $\overline{\mathbf{q}_0\mathbf{q}_k} \notin \mathcal{B}_0$  do not have to be in a collision (e.g., spines  $\overline{\mathbf{q}_0\mathbf{q}_4}, \dots, \overline{\mathbf{q}_0\mathbf{q}_{10}}$  from Fig. 4 (a)). Therefore, to further explore free space beyond  $\mathcal{B}_0$ , Alg. 4 proposes the following:

**Step 1** (lines 3–4): For the current root configuration  $\mathbf{q}_k$ , compute a bur  $Bur_k$  by checking nodes from  $\pi[\mathbf{q}_k, \mathbf{q}_f]$ ,  $\forall k \in \{m, \dots, N-1\}$ , for some  $m \in \{0, \dots, N-1\}$ , for membership in  $\mathcal{B}(\mathbf{q}_k, \mathbf{d}(\mathbf{q}_k))$  (e.g., black spines from  $\mathbf{q}_0$  towards  $\mathbf{q}_1, \mathbf{q}_2, \mathbf{q}_3 \in \mathcal{B}_0$ , and from  $\mathbf{q}_3$  towards  $\mathbf{q}_4, \mathbf{q}_5, \mathbf{q}_6 \in \mathcal{B}_3$  in Fig. 4 (a)). If  $Bur_k$  exists, continue to subsequent steps. Otherwise, return all burs computed so far.

**Step 2** (lines 5–6): Let  $\mathbf{q}_m$  be the last node in the current bur  $Bur_k$ . Use  $\mathbf{q}_m$  as the root for a new bubble  $\mathcal{B}_m$  (e.g.,  $\mathbf{q}_3$  and  $\mathbf{q}_6$  become the root of  $\mathcal{B}_3$  and  $\mathcal{B}_6$  in Fig. 4 (a), respectively).

**Step 3** (line 7): While computing distance to obstacles  $d_{i,j}$ , nearest points  $R_{i,j}$  and  $O_{i,j}$  between  $i$ -th robot’s link and  $j$ -th obstacle  $\mathcal{W}\mathcal{O}_j$  can be obtained. They define a separating plane  $P_{i,j}$  dividing free/occupied halfspaces as proven in [26]. After the robot moves from  $\mathbf{q}_k$  to  $\mathbf{q}_m$ , new underestimates of  $d_{i,j}$  can be easily acquired as a distance to  $P_{i,j}$  when the robot assumes  $\mathbf{q}_m$  (e.g.,  $\mathbf{q}_3$  and  $\mathbf{q}_6$  in Fig. 4 (c, d)). All  $P_{i,j}$  are stored within a matrix  $\mathcal{P}$ .

**Step 4** (line 8): Concatenate all spines from each bur  $Bur_k$  into a single structure called  $GBur$  (generalized  $Bur$ , see [26] for details). Repeat steps 1–4 until  $\mathbf{q}_k = \mathbf{q}_f$  or no new bur can be formed (e.g.  $Bur_6$  in Fig. 4 (a)).

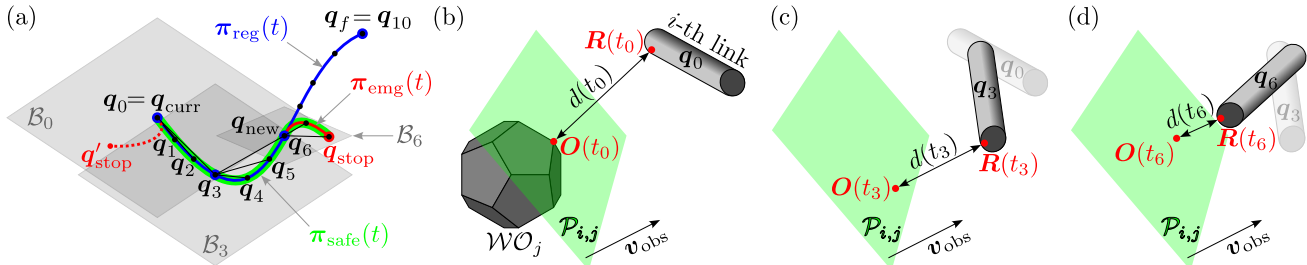


Fig. 4: (a) Process of computing generalized bur (solid black lines); (b,c,d) The nearest points,  $\mathbf{R}(t) \equiv \mathbf{R}_{i,j}(t)$  and  $\mathbf{O}(t) \equiv \mathbf{O}_{i,j}(t)$ , from  $i$ -th robot's link and  $\mathcal{W}\mathcal{O}_j$ , with the corresponding plane  $\mathcal{P}_{i,j} \equiv \mathcal{P}_{i,j}(t)$  and the distance  $d(t) \equiv d_{i,j}(t)$  after  $t \in \{t_0, t_3, t_6\}$ .

## B. Safe Trajectories

For DEs, safety guarantees via *dynamic expanded bubbles of free C-space (DEBs)* under an upper bound on obstacle velocity  $v_{obs}$  can be provided as in [24]. Here, it is assumed that each plane  $\mathcal{P}_{i,j}$  moves toward  $i$ -th robot's link at a constant, worst-case speed  $v_{obs} = \|\mathbf{v}_{obs}\|$  (see Fig. 4 (b)–(d)). Thus, when checking whether a configuration  $\mathbf{q}(t) \in DEB$ , the distance  $d_c$  in (3) is reduced by the plane's traversed path length  $v_{obs} \cdot (t - t_0)$ .

Moreover, after reaching the configuration  $\mathbf{q}_{new}$ , which represents the border of the last generated bubble, emergency (quartic) spline  $\pi_{emg}(t) = \pi[\mathbf{q}_{new}, \mathbf{q}_{stop}]$  is computed. Thus, the robot can stop in a new configuration  $\mathbf{q}_{stop}$  as needed (e.g., the red spline from  $\mathbf{q}_6$  in Fig. 4 (a)). If  $\pi_{emg}(t)$  is collision-free, a *local safe trajectory*, defined as  $\pi_{safe}(t) = \pi[\mathbf{q}_{curr}, \mathbf{q}_{new}] \cup \pi_{emg}(t)$ , can be followed from the current iteration (e.g., the green trajectory in Fig. 4 (a)). Otherwise, the robot can execute emergency stopping from  $\mathbf{q}_{curr}$ , which was computed at the planner's previous iteration (e.g., stopping at  $\mathbf{q}'_{stop}$  depicted by the dashed red line in Fig. 4 (a)). To summarize, CFS45 method distinguish two trajectory types:

- Regular trajectory – a sequence of quintic splines which are not a priori guaranteed to be safe (i.e., collision of those splines is not checked). Theoretically, the robot can be in motion at the time instance of collision (type I collision);
- Safe trajectory – a sequence of quintic and quartic (emergency) splines lying inside a chain of connected *DEBs*. By following those splines, the robot is always located at a safe configuration. Any collision, should it occur, is constrained to happen only if the robot's velocity is zero (type II collision) – see [24] for more details.

## VII. SIMULATION STUDY

This section provides an extensive simulation study<sup>1</sup> with two distinct goals. The first goal is to measure the execution time required for generating “random” trajectories during the randomized trial scenarios. Another goal is to conduct a benchmark where we compare our method to the state-of-the-art Ruckig method [18] within two sampling-based planning approaches tailored for DEs. This competitor is selected primarily due to its computational efficiency, code availability, and the additional relevant features from Tab. I.

<sup>1</sup>The implementation of CFS45 method in C++ is available in the supplementary material. Moreover, the incorporation of Ruckig library can be found there in `TrajectoryRuckig` class. The simulation was performed using the laptop PC with Intel® Core™ i7-9750H CPU @ 2.60 GHz  $\times$  12 with 16 GB of RAM, with the code compiled to run on a single core of the CPU without any GPU acceleration.

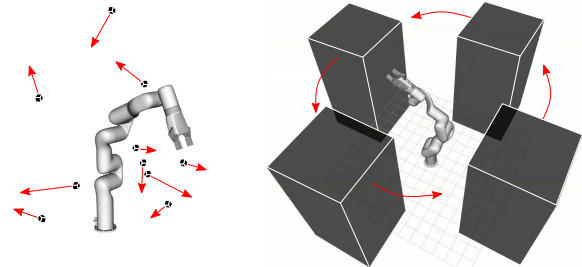


Fig. 5: Two used scenarios: Scenario 1 (left) – ten small random obstacles, and Scenario 2 (right) – four large predefined obstacles. Motion of obstacles is depicted by the red velocity vectors.

For planning we employ two approaches: a simple online version of RRT-like algorithm (ORRT), and a more recent algorithm specifically dedicated to DEs (DRGBT) [24]. ORRT tries to extend from  $\mathbf{q}_{curr}$  toward  $\mathbf{q}_{target}$ . Extensions are achieved only when the straight-line connection  $\overline{\mathbf{q}_{curr}\mathbf{q}_{target}}$  is determined to be collision-free, where  $\mathbf{q}_{target}$  can be equal to  $\mathbf{q}_{goal}$  or a randomly sampled configuration  $\mathbf{q}_{rand}$ .

### A. Scenario Setup

The simulation study deals with 19 scenario types, with each type using the planner's iteration time  $T \in \{1, 2, 3, \dots, 10, 20, 30, \dots, 100\}$  [ms]. This time determines the frequency of generating a new trajectory from  $\mathbf{q}_{curr}$  toward a (possibly) new  $\mathbf{q}_{target}$ . Fig. 5 illustrates two scenarios used in the simulation study. The first one consists of ten random obstacles, where each one is assigned a random velocity with its magnitude limited to  $1.6 \frac{m}{s}$ . The second scenario uses four large obstacles moving at a random speed up to  $0.3 \frac{m}{s}$ .

The model of the UFactory xArm6 robot is exposed to 1000 different simulation runs with randomly generated circumstances (i.e., 1000 random but collision-free start and goal configurations). We opted to use quintic splines ( $m = 5$ ) within our approach since the real xArm6 manipulator has to meet constraints  $\mathcal{K}$  on maximal joint  $\mathbb{V}$ ,  $\mathbb{A}$ , and  $\mathbb{J}$ . These values are:  $\omega_{max} = \pi_{n \times 1} \frac{[rad]}{[s]}$ ,  $\alpha_{max} = 20_{n \times 1} \frac{[rad]}{[s^2]}$ , and  $j_{max} = 500_{n \times 1} \frac{[rad]}{[s^3]}$ , respectively, taken from the datasheet of xArm6 robot. For the sake of completeness, we carry out simulations for both types of trajectories (regular and safe), as defined in Sec. VI.

### B. Comparison with Ruckig

Fig. 6 shows an example of generated trajectories by both CFS45 and Ruckig approaches for a planar 2-DoF manipulator which is guided by DRGBT algorithm with  $T = 50$  [ms]. Black dots designate points in each planner's iteration, while dotted red/blue curves depict generated local trajectories in

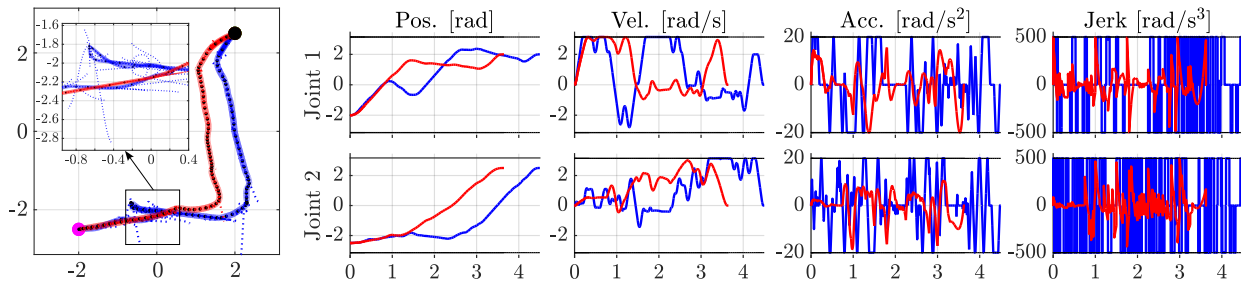


Fig. 6: An example of generated trajectories (in  $\{q_1, q_2\}$ -plane on the left and joint  $\mathbb{P}$ ,  $\mathbb{V}$ ,  $\mathbb{A}$ , and  $\mathbb{J}$  functions in time [s] on the right hand side) by both **CFS45** and **Ruckig** approaches for a planar 2-DoF robotic manipulator. Black lines depict minimum/maximum values.

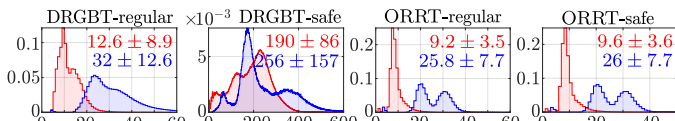


Fig. 7: PDFs constructed for execution times in  $[\mu\text{s}]$  of generating trajectories using **CFS45** and **Ruckig** methods. Mean and standard deviation times are indicated in corresponding subfigures.

each iteration. The accompanying video shows more scenarios operating in real time for regular and safe trajectories generated by both Ruckig and the proposed algorithm.

Fig. 6 also illustrates  $\mathbb{P}$ ,  $\mathbb{V}$ ,  $\mathbb{A}$ , and  $\mathbb{J}$  responses. Clearly, both methods satisfy all kinematic constraints and successfully reach the goal. In terms of smoothness (captured via jerk L1-norm), the proposed approach displays more desirable behavior with the average of 3.3 times improvement. Moreover, for the conducted scenarios, the proposed approach shows in average 2.33 times lower Frechet distance [27], which is computed in each iteration as a “distance” between the line segment  $\bar{\mathbf{q}}_{\text{curr}}\mathbf{q}_{\text{target}}$  and the geometric path resulting from the computed trajectory  $\pi[\mathbf{q}_{\text{curr}}, \mathbf{q}_{\text{target}}]$ .

Fig. 7 depicts probability density functions (PDFs) of execution times required for generating trajectories using CFS45 and Ruckig methods by four dynamic planners: DRGBT-regular/safe and ORRT-regular/safe. Clearly, the proposed method completes almost 3 times faster than Ruckig. It is worth mentioning that each histogram contains more than 24 million of data (different “random” trajectories).

Finally, Fig. 8 reveals the performance of DRGBT-regular/safe and ORRT-regular/safe methods when using CFS45 and Ruckig approaches as trajectory generator. The performance is defined by the following criteria used for the comparison: (adjusted) success rate, algorithm time (required time for the robot to reach the goal), and path length from the start to the goal. Opposing to the classic success which is binary (1 if the goal is reached, and 0 otherwise), the *adjusted success* is measured as a proxy for each run using the real number  $1 - \frac{\|\mathbf{q}_{\text{end}} - \mathbf{q}_{\text{goal}}\|}{\|\mathbf{q}_{\text{start}} - \mathbf{q}_{\text{goal}}\|} \in [0, 1]$ , where  $\mathbf{q}_{\text{end}}$  represents an end configuration (in case of collision, it is a configuration at which the collision occurred, otherwise  $\mathbf{q}_{\text{end}} = \mathbf{q}_{\text{goal}}$ ). After averaging all adjusted successes for each run, we obtain the *adjusted success rate*. Clearly, Fig. 8 shows that CFS45 outperforms Ruckig according to all criteria. Particularly, considerable performance improvement is achieved at higher planner frequencies (above 100 [Hz], i.e., for  $T \leq 10$  [ms]).

## VIII. EXPERIMENTAL VALIDATION

To validate the proposed CFS45 method in both static and dynamic environments (i.e., in the presence of human), we

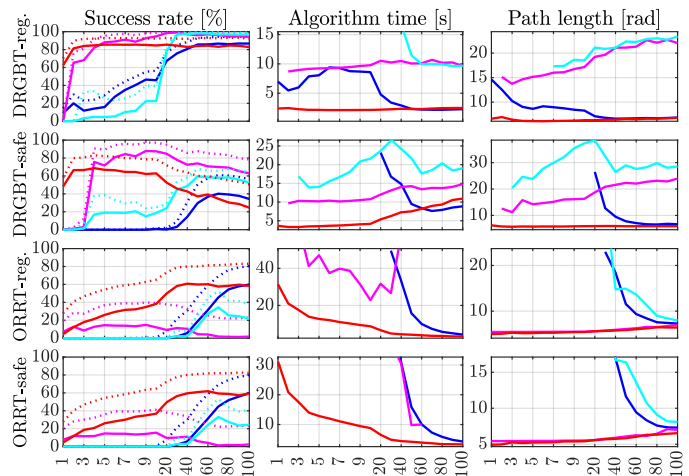


Fig. 8: The performance of the used dynamic planners in cases: **CFS45** for **Scenario 1** and **Ruckig** for **Scenario 1**; **CFS45** for **Scenario 2** and **Ruckig** for **Scenario 2**. Dashed line depicts adjusted success rate. Algorithm time and path length are not shown in cases when success rate is less than 10 [%] or in cases when they are greater than the shown plot limits.

conduct four experiments on the real UFACTORY xArm6 manipulator. Environment sensing is performed with two *Intel RealSense D435i* depth cameras operating at  $f_{\text{perc}} = 20$  [Hz]. The perception pipeline fuses the left and right point clouds into a single unified one to extract obstacles as axis-aligned bounding boxes. To facilitate collision and distance queries, the robot links are approximated by bounding capsules. The low-level controller operates at  $f_{\text{con}} = 500$  [Hz] handling the desired and measured  $\mathbb{P}$  and  $\mathbb{V}$  for each joint.

The planning algorithm runs within a ROS2 environment, where the implementation is publicly available in the supplementary material. The planner outputs a desired trajectory (containing  $\mathbb{P}$ ,  $\mathbb{V}$ , and  $\mathbb{A}$  for each joint) with the frequency  $f_{\text{alg}} = 1/T$  (we use  $f_{\text{alg}} = 20$  [Hz] to be synchronized with  $f_{\text{perc}}$ ). Since  $f_{\text{alg}}$  is usually different from  $f_{\text{con}}$ , the obtained trajectory can be sampled with  $f_{\text{con}}$ , and then passed to the controller with the corresponding samples in order to achieve a smooth motion of the robot.

The accompanying video demonstrates a successful execution of both regular and safe trajectories for different jerk limits (e.g.,  $50 \frac{\text{rad}}{\text{s}^3}$  and  $200 \frac{\text{rad}}{\text{s}^3}$ ). Representative snapshots are shown in Fig. 9, where the path traversed by the end-effector is depicted by red lines. The measured  $\mathbb{P}$  and  $\mathbb{V}$  for each joint are given in Fig. 10. Clearly, all velocities remain within the set limits of  $1.5 \frac{\text{rad}}{\text{s}}$  for each joint. Unfortunately, the used robot does not provide measurements of joint accelerations.

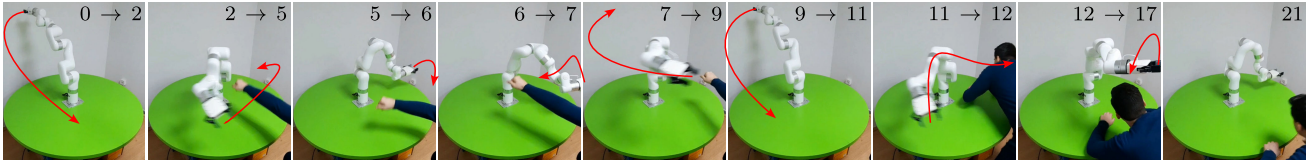


Fig. 9: Snapshots from the real-world scenario. Time transition in [s] is depicted in each snapshot.

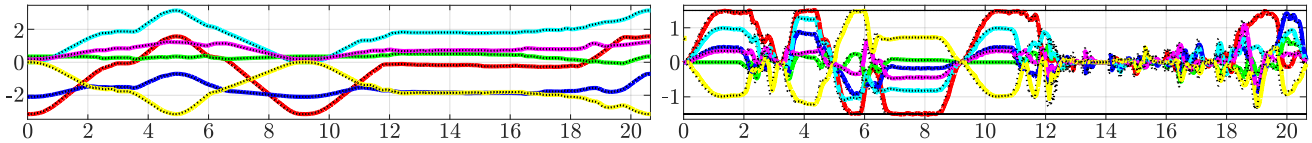


Fig. 10: Measured position [rad] (left) and velocities [ $\frac{\text{rad}}{\text{s}}$ ] (right) for each joint (Joint 1, Joint 2, Joint 3, Joint 4, Joint 5, Joint 6) from the scenario in Fig. 9. All referent functions are shown by black dotted lines.

## IX. CONCLUSION

We presented an online method for converting arbitrary geometric paths into jerk-limited, kinematically-feasible trajectories using sequences of quintic/quartic splines. The approach accounts for all the kinematic constraints up to limited jerks. The procedure interpolates safe trajectories and provides safety guarantees in both static and dynamic environments.

Moreover, a comprehensive simulation comparison against the state-of-the-art approach demonstrates significant improvement in performance considering trajectory smoothness, computational efficiency, and dynamic planner's frequency. Experimental validation confirms the proposed approach is suitable for real-world scenarios including human presence.

Future work will include validation of the novel method on a different types of robots (e.g., mobile robots). Moreover, robots with many DoFs will be used to inspect how the proposed approach scales with the increased dimensionality.

## REFERENCES

- [1] J. E. Bobrow, S. Dubowsky, and J. S. Gibson, "Time-optimal control of robotic manipulators along specified paths," *The international journal of robotics research*, vol. 4, no. 3, pp. 3–17, 1985.
- [2] K. Shin and N. McKay, "Minimum-time control of robotic manipulators with geometric path constraints," *IEEE Transactions on Automatic Control*, vol. 30, no. 6, pp. 531–541, 1985.
- [3] H. Pham and Q.-C. Pham, "A new approach to time-optimal path parameterization based on reachability analysis," *IEEE Transactions on Robotics*, vol. 34, no. 3, pp. 645–659, 2018.
- [4] D. Verschuere, B. Demeulenaere, J. Swevers, J. De Schutter, and M. Diehl, "Time-optimal path tracking for robots: A convex optimization approach," *IEEE Transactions on Automatic Control*, vol. 54, no. 10, pp. 2318–2327, 2009.
- [5] S. Macfarlane and E. A. Croft, "Jerk-bounded manipulator trajectory planning: Design for real-time applications," *IEEE Transactions on robotics and automation*, vol. 19, no. 1, pp. 42–52, 2003.
- [6] H. Zhao, N. Abdurahiman, N. Navkar, J. Leclerc, and A. T. Becker, "Jerk-continuous online trajectory generation for robot manipulator with arbitrary initial state and kinematic constraints," in *2022 IEEE/RSJ International Conference on Intelligent Robots and Systems (IROS)*. IEEE, 2022, pp. 5730–5736.
- [7] W. Yu, D. Qu, F. Xu, L. Zhang, F. Zou, and Z. Du, "Time-optimal multi-point trajectory generation for robotic manipulators with continuous jerk and constant average acceleration," *Control Engineering Practice*, vol. 154, p. 106154, 2025.
- [8] J.-E. Lee, A. Bylard, R. Sun, and L. Sentis, "On the performance of jerk-constrained time-optimal trajectory planning for industrial manipulators," in *2024 IEEE International Conference on Robotics and Automation (ICRA)*. IEEE, 2024, pp. 9772–9778.
- [9] M. Wang, J. Xiao, F. Zeng, and G. Wang, "Research on optimized time-synchronous online trajectory generation method for a robot arm," *Robotics and Autonomous Systems*, vol. 126, p. 103453, 2020.
- [10] Y. Xu, Y. Liu, X. Liu, J. Cao, and L. Zhang, "Segmented dynamic adaptive look-ahead smoothing feedrate scheduling with joint jerk constraints of 6r robot manipulators," *IEEE Transactions on Automation Science and Engineering*, vol. 22, pp. 7033–7051, 2024.
- [11] F. Lange and A. Albu-Schäffer, "Path-accurate online trajectory generation for jerk-limited industrial robots," *IEEE Robotics and Automation Letters*, vol. 1, no. 1, pp. 82–89, 2015.
- [12] Y. Wen and P. Pagilla, "Path-constrained and collision-free optimal trajectory planning for robot manipulators," *IEEE Transactions on Automation Science and Engineering*, vol. 20, no. 2, pp. 763–774, 2022.
- [13] P. Holmes, S. Kousik, B. Zhang, D. Raz, C. Barbalata, M. Johnson-Roberson, and R. Vasudevan, "Reachable sets for safe, real-time manipulator trajectory design," in *Proceedings of Robotics: Science and Systems (RSS)*, 2020.
- [14] A. Pupa, M. Arrfou, G. Andreoni, and C. Secchi, "A safety-aware kinodynamic architecture for human-robot collaboration," *IEEE Robotics and Automation Letters*, vol. 6, no. 3, pp. 4465–4471, 2021.
- [15] B. Sundaralingam, S. K. S. Hari, A. Fishman, C. Garrett, K. Van Wyk, V. Blukis, A. Millane, H. Oleynikova, A. Handa, F. Ramos *et al.*, "Curobo: Parallelized collision-free robot motion generation," in *2023 IEEE International Conference on Robotics and Automation (ICRA)*. IEEE, 2023, pp. 8112–8119.
- [16] K. Patra, A. Sinha, and A. Guha, "Kinodynamic motion planning for collaborative object transportation by multiple mobile manipulators," *Journal of Mechanisms and Robotics*, vol. 17, no. 12, p. 121003, 2025.
- [17] T. Kröger and F. M. Wahl, "Online trajectory generation: Basic concepts for instantaneous reactions to unforeseen events," *IEEE Transactions on Robotics*, vol. 26, no. 1, pp. 94–111, 2009.
- [18] L. Berscheid and T. Kroeger, "Jerk-limited Real-time Trajectory Generation with Arbitrary Target States," in *Proceedings of Robotics: Science and Systems*, Virtual, July 2021.
- [19] J.-M. Lien and N. M. Amato, "Approximate convex decomposition of polyhedra and its applications," *Computer Aided Geometric Design*, vol. 25, no. 7, pp. 503–522, 2008.
- [20] S. Quinlan, *Real-time modification of collision-free paths*. Stanford University Stanford, 1994, no. 1537.
- [21] J. J. Kuffner and S. M. LaValle, "RRT-Connect: An efficient approach to single-query path planning," in *Proceedings 2000 ICRA. Millennium Conference. IEEE International Conference on Robotics and Automation.*, vol. 2. IEEE, 2000, pp. 995–1001.
- [22] M. Otte and E. Frazzoli, "RRT\*: Asymptotically optimal single-query sampling-based motion planning with quick replanning," *The International Journal of Robotics Research*, vol. 35, no. 7, pp. 797–822, 2016.
- [23] C. Tonola, M. Faroni, M. Beschi, and N. Pedrocchi, "Anytime informed multi-path replanning strategy for complex environments," *IEEE Access*, vol. 11, pp. 4105–4116, 2023.
- [24] N. Covic, B. Lacevic, D. Osmankovic, and T. Uzunovic, "Real-time sampling-based safe motion planning for robotic manipulators in dynamic environments," *IEEE Transactions on Robotics*, 2025.
- [25] A. Ademovic and B. Lacevic, "Path planning for robotic manipulators using expanded bubbles of free C-space," in *2016 IEEE International Conference on Robotics and Automation (ICRA)*, 2016, pp. 77–82.
- [26] B. Lacevic and D. Osmankovic, "Improved C-space exploration and path planning for robotic manipulators using distance information," in *2020 IEEE International Conference on Robotics and Automation (ICRA)*. IEEE, 2020.
- [27] H. Alt and M. Godau, "Computing the Fréchet distance between two polygonal curves," *International Journal of Computational Geometry & Applications*, vol. 5, pp. 75–91, 1995.